Mark TJ Lin et al. / International Journal of Automotive Engineering
Vol.13, No.4(2022)
Research Paper
20224548

Race Car Aerodynamics Simulation and Transmitted Tire Reaction Forces

Mark TJ Lin [1)] Periklis Papadopoulos [1)]

1) San Jose State University, Department of Aerospace Engineering
1 Washington Square, San Jose, CA 95192, USA (E-mail: mark.lin@sjsu.edu, marklin1188@yahoo.com)

Received on March 8 ,2022

ABSTRACT: Often in Computational Fluid Dynamics integral forces and restoring moments are calculated, but the location where they should be applied may not always be clear. This is because the location is not intuitive: it is dependent on the vehicle's velocity and its orientation (e.g. sideslip angle). A technique has been developed to translate the aerodynamic forces to the reaction forces on the vehicle's tires. In this study, CFD simulation is performed with a 7.5° yaw to look at the effect of cornering. To understand aerodynamic effect on vehicle dynamics one must know the location at which this force is applied. This location is commonly called the center of pressure (COP), but more precisely it should be called the COP-Axis because the force is applied along a line-of-action rather than a point. This paper illustrates that.
After knowing the aerodynamic forces and the COP-Axis, the reaction force at each tire is calculated. First, the problem is modeled up as a single force with 4 tires. As one can guess, having 4 tires is over-constraining so this is a static indeterminant problem. In 3D there are 6 equations but now we have 12 unknowns. In order to solve the static indeterminant problem it is modelled up as a deformable body. By taking material property into consideration, the percentage of load that's transferred to each tire is affected. Using the process described in this paper, reaction forces from each tire have been successfully computed and one can see their effect from aerodynamic loads.

KEY WORDS: COP-Axis, External aerodynamics, CFD, Static indeterminate, Nonlinear, Vehicle dynamics [D1]

1. Introduction

In this paper, a method to compute tire reaction forces from the applied aerodynamic force is presented. Here, three car geometries are used as examples to illustrate, and also used to verify this computation process. Two of the three car geometries have been published previously. The first geometry is Ferrari's Formula 1 car SF70H/71H; the second geometry is Team Williams' Formula 1 car FW42; the third geometry is San Jose State University's Formula SAE car SR-12B, which the author was involved in constructing at SJSU as a team member.

Most people know how to compute drag, downforce, and side force (with some tricks) in CFD; but in order to make this data meaningful, as well as useful, two questions need to be answered. First, where is this force applied? And second, how is this force transmitted to the four tires that are contacting the ground? [(1)]

The problem of computing drag, downforce, and side force for complex geometries has been discussed in previous publications. In this paper, a method for calculating the tire reaction forces is presented.

2. Methods of Approach

2.1. Static calculation using sum of moments

In static calculation, we can sum forces and we can sum moments. In 3D, we have 6 independent equations that we can use to solve for 6 unknowns (and each component force is one unknown) [(2)].

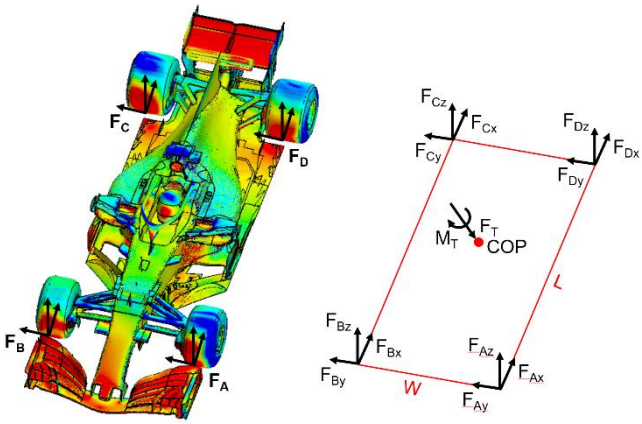

Fig. 1 Free body diagram.

First we sum forces, and we have 3 component equations summing the reaction forces from each tire. This gives us the familiar form that's shown in Equations 1A-C.

$$\sum F = 0$$

$$F_{Ax} + F_{Bx} + F_{Cx} + F_{Dx} + Drag = 0 \quad (1A)$$

$$F_{Ay} + F_{By} + F_{Cy} + F_{Dy} + SideForce = 0 \quad (1B)$$

$$F_{Az} + F_{Bz} + F_{Cz} + F_{Dz} + Downforce = 0 \quad (1C)$$

Next, we sum moments. Let's write the moment equation about tire *C*. Here in Equation 2, F_A, F_B, and F_D, are the reaction forces at tire *A*, *B*, and *D*. F_T is the externally applied aerodynamic force, namely the drag, side force, and downforce [(3)]. To calculate its moment about tire *C*, the moment arm for F_T is the position vector from tire *C* to the *COP* location that is reported by the CFD software. And M_T is the residual moment about the F_T force vector.

Note: the moment equation is a vector equation so it comprises of the 3 components *x*, *y*, and *z* therefore this already represents the other 3 independent equations we have.

$$\sum M_c = 0$$
$$\left(\overrightarrow{CA} \times \overrightarrow{F_A}\right) + \left(\overrightarrow{CB} \times \overrightarrow{F_B}\right) + \left(\overrightarrow{CD} \times \overrightarrow{F_D}\right) + \left(\overrightarrow{CCOP} \times \overrightarrow{F_T}\right) + \overrightarrow{M_T} = 0 \quad (2)$$

Carrying out the vector cross product, Equations 3-7 shows the moment from each term in Equation 2 [4]. Putting them together and writing it out in component form we will obtain Equation 8.

$$\overrightarrow{CA} \times \overrightarrow{F_A} = \begin{vmatrix} \hat{\imath} & \hat{\jmath} & \hat{k} \\ -L & -W & 0 \\ F_{Ax} & F_{Ay} & F_{Az} \end{vmatrix} = -WF_{Az}\hat{\imath} + LF_{Az}\hat{\jmath} + \left(-LF_{Ay} + WF_{Ax}\right)\hat{k} \quad (3)$$

$$\overrightarrow{CB} \times \overrightarrow{F_B} = \begin{vmatrix} \hat{\imath} & \hat{\jmath} & \hat{k} \\ -L & 0 & 0 \\ F_{Bx} & F_{By} & F_{Bz} \end{vmatrix} = LF_{Bz}\hat{\jmath} - LF_{By}\hat{k} \quad (4)$$

$$\overrightarrow{CD} \times \overrightarrow{F_D} = \begin{vmatrix} \hat{\imath} & \hat{\jmath} & \hat{k} \\ 0 & -W & 0 \\ F_{Dx} & F_{Dy} & F_{Dz} \end{vmatrix} = -WF_{Dz}\hat{\imath} + WF_{Dx}\hat{k} \quad (5)$$

$$\overrightarrow{CCOP} = (-L + COP_x)\hat{\imath} + \left(-\frac{W}{2} + COP_y\right)\hat{\jmath} + COP_z\hat{k} \quad (6)$$

$$\overrightarrow{CCOP} \times \overrightarrow{F_T} = \begin{vmatrix} \hat{\imath} & \hat{\jmath} & \hat{k} \\ (-L + COP_x) & \left(-\frac{W}{2} + COP_y\right) & COP_z \\ Drag & SideForce & Downforce \end{vmatrix} = N_1\hat{\imath} + N_2\hat{\jmath} + N_3\hat{k} \quad (7)$$

Here, N_1, N_2, N_3 are the calculated constant coefficients. Writing Equation 2 out by components and substituting-in Equations 3-7, we would get the component forms shown in Equations 8A, 8B, and 8C:

$$\hat{\imath}: \; -WF_{Az} - WF_{Dz} + N_1 + M_{Tx} = 0 \quad (8A)$$
$$\Rightarrow \; F_{Az} + F_{Dz} = \frac{N_1 + M_{Tx}}{W}$$
$$\hat{\jmath}: \; LF_{Az} + LF_{Bz} + N_2 + M_{Ty} = 0 \quad (8B)$$
$$\Rightarrow \; F_{Az} + F_{Bz} = -\left(\frac{N_2 + M_{Ty}}{L}\right)$$
$$\hat{k}: \; -LF_{Ay} + WF_{Ax} - LF_{By} + WF_{Dx} + N_3 + M_{Tz} = 0 \quad (8C)$$

Here, using static analysis we obtain solution of the reaction forces in pairs, for example $F_{Az} + F_{Dz}$ because we don't have enough equations to solve for each individual unknown. But this is still useful because we can use it to determine the aero balance, which is defined as the ratio of downforce distributed between the front two tires versus the rear two tires, or the inside two tires versus the outside two tires [5–8].

From Equation 8B we already have the combined front tire forces.

$$\%\, front\ tires = \frac{F_{Az} + F_{Bz}}{Downforce} \quad (9)$$

From Equation 8A, $F_{Az} + F_{Dz}$ is the outside tire force; but since we have Equation 1C, we can subtract them and find the inside tire force $F_{Bz} + F_{Cz}$.

$$F_{Az} + F_{Bz} + F_{Cz} + F_{Dz} + Downforce = 0$$
$$\Rightarrow F_{Bz} + F_{Cz} = -Downforce - (F_{Az} + F_{Dz})$$
$$= -Downforce - \frac{N_1 + M_{Tx}}{W} \quad (10)$$
$$\%\, inside\ tires = \frac{F_{Bz} + F_{Cz}}{Downforce} \quad (11)$$

2.2. Solid mechanics calculation of deformable body

While the foregoing analysis yield useful results, we want to go further and derive the reaction force for each individual tire. To do this, we had to use solid mechanics and write the equations in terms of internal forces and body deformation; in other words, solving it by statics alone will not get us there.

In solid mechanics, which we distinguish from fluid mechanics and CFD, two concepts are enforced: equilibrium and compatibility [9]. Equilibrium is the sense that all forces, both internal and external, sum to zero. There are no net force acting on the body and therefore the body is in equilibrium. Compatibility is the sense that deformation in each of the members must be equal and consistent so that the structural body does not fall apart.

For this problem, in order to write the deformation equation for compatibility, we have to idealize the geometry into a simpler structure that we can analyze. While the external shape we used in CFD gave us external forces, how that force is transmitted to the tires is all done by internal structural members. For tube-frame cars like SJSU's SR-12B this is done by the chassis steel tubes, while for Formula 1 cars it is done by the carbon composite monocoque which is a complex geometry. In order to analyze the problem, we chose a simplified structural geometry as shown in Figure 2. We call this geometry the pyramid model, which is simply four rods connected at the location where the external force is applied to each of the four tires. Each rod, or legs as we'll refer to later, has an axial stiffness *EA*, where *E* is the Young's modulus and *A* is the cross sectional area of the rod. Instead of using the pyramid model, a fancier way to incorporate the deformation would be to analyze the actual geometry using FEA and come up with an equivalent stiffness in each of the legs, but that is left to the reader.

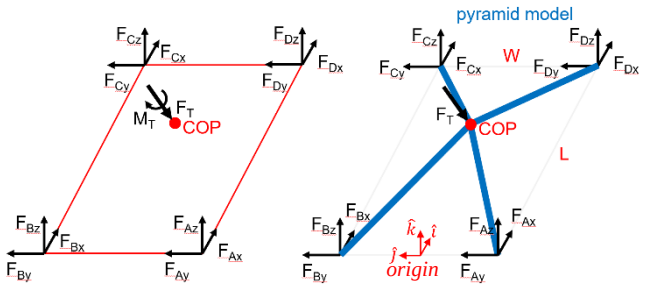

Fig. 2 Pyramid model.

For equilibrium condition, the equations take a similar form to Equations 1A-C of the static analysis. The only difference here is now we write it as internal force magnitude times the direction unit vector of each leg.

$$\sum F = 0$$
$$F_A\hat{a} + F_B\hat{b} + F_C\hat{c} + F_D\hat{d} + \overrightarrow{F_T} = 0 \quad (12)$$

where $\hat{a}$ is the unit vector of leg A, $\hat{b}$ is the unit vector of leg B, $\hat{c}$ is the unit vector of leg C, and $\hat{d}$ is the unit vector of leg D. And F_A, F_B, F_C, and F_D are the magnitude of internal forces within each leg.

Here, the internal forces are positive if the leg is in tension, and negative if in compression. The direction of the tire reaction forces are as shown in Figure 2. The *Drag*, *SideForce*, and *Downforce* are in the center coordinate frame (i.e. *Drag* is +ve, *SideForce* is -ve, and *Downforce* is -ve).

Writing it out in components they become scalar equations, and $(a_x, a_y, a_z), (b_x, b_y, b_z), (c_x, c_y, c_z)$, and (d_x, d_y, d_z) are the component of the unit vectors.

$$\begin{cases} \hat{\imath}\text{: } F_A a_x + F_B b_x + F_C c_x + F_D d_x + Drag = 0 \\ \hat{\jmath}\text{: } F_A a_y + F_B b_y + F_C c_y + F_D d_y + SideForce = 0 \\ \hat{k}\text{: } F_A a_z + F_B b_z + F_C c_z + F_D d_z + Downforce = 0 \end{cases} \quad (13)$$

For compatibility condition, the equations are shown in Equations 14-17. They are basically four equations that say the new length of each leg is equal to the original length of each leg plus their deformations δ [10]. Here the prime variables indicate the new lengths and the new COP location. *A*, *B*, *C*, and *D* denote the location of the four tires. They are written in the *center coordinate system*, which we define as the center of the front axel (i.e. mid-distance between the two front tires). These four equations are also scalar equations.

$$\begin{aligned} & l'_A = l_A + \delta_A \\ & \sqrt{(COP'_x - A_x)^2 + \left(COP'_y - A_y\right)^2 + (COP'_z - A_z)^2} = l_A + \delta_A \\ & \sqrt{(COP'_x - 0)^2 + \left(COP'_y - \left(-\frac{W}{2}\right)\right)^2 + (COP'_z - 0)^2} \\ & \qquad = l_A + \frac{l_A F_A}{EA} \end{aligned} \quad (14)$$

$$\begin{aligned} & l'_B = l_B + \delta_B \\ & \sqrt{(COP'_x - B_x)^2 + \left(COP'_y - B_y\right)^2 + (COP'_z - B_z)^2} = l_B + \delta_B \\ & \sqrt{(COP'_x - 0)^2 + \left(COP'_y - \frac{W}{2}\right)^2 + (COP'_z - 0)^2} = l_B + \frac{l_B F_B}{EA} \end{aligned} \quad (15)$$

$$\begin{aligned} & l'_C = l_C + \delta_C \\ & \sqrt{(COP'_x - C_x)^2 + \left(COP'_y - C_y\right)^2 + (COP'_z - C_z)^2} = l_C + \delta_C \\ & \sqrt{(COP'_x - L)^2 + \left(COP'_y - \frac{W}{2}\right)^2 + (COP'_z - 0)^2} = l_C + \frac{l_C F_C}{EA} \end{aligned} \quad (16)$$

$$\begin{aligned} & l'_D = l_D + \delta_D \\ & \sqrt{(COP'_x - D_x)^2 + \left(COP'_y - D_y\right)^2 + (COP'_z - D_z)^2} = l_D + \delta_D \\ & \sqrt{(COP'_x - L)^2 + \left(COP'_y - \left(-\frac{W}{2}\right)\right)^2 + (COP'_z - 0)^2} \\ & \qquad = l_D + \frac{l_D F_D}{EA} \end{aligned} \quad (17)$$

In this system of four compatibility equations, the unknowns are COP'_x, COP'_y, COP'_z, and the internal forces F_A, F_B, F_C, F_D inside each member (*the parameters EA is the axial stiffness so it's a constant)*. However, we can use the equilibrium conditions expressed in three scalar equations in Equation 13 to eliminate the force variables and combine the four compatibility equations into three. In these three equations there are only three unknowns COP'_x, COP'_y, and COP'_z so we can solve for them.

In other words, between equilibrium and compatibility we have seven equations (Equations 13-17). There are seven unknowns, namely COP'_x, COP'_y, COP'_z, F_A, F_B, F_C, and F_D. Hence we can solve for them. In short, the three equilibrium equations (Equation 13) can be recast into expressions relating two unknowns, for example F_A and F_B. Next, we substitute that expression into Equation 14 and rewrite it in terms of F_B. Then we subtract Equation 15 from Equation 14 to eliminate F_B. Finally, what we are left with is Equation 18A.

The three combined equations we solve are shown in Equation 18A-C. Here $N_4 \sim N_{12}$ are computed constants. Looking at these three equations, they represent a system of nonlinear equations that is difficult to solve analytically. The way we solve these three equations for COP_x', COP_y', and COP_z' is by numerical means: namely, writing the equations into a spreadsheet; computing the LHS (left hand side) and RHS (right hand side) separately, and iterate through a point-cloud (i.e. grid array) that minimizes the error between the LHS and the RHS.

$$N_4 \sqrt{COP'^2_x + \left(COP'_y + \frac{W}{2}\right)^2 + COP'^2_z} + \sqrt{COP'^2_x + \left(COP'_y - \frac{W}{2}\right)^2 + COP'^2_z} = N_5 - \frac{N_6}{EA} \quad (18A)$$

$$N_7 \sqrt{(COP'_x - L)^2 + \left(COP'_y + \frac{W}{2}\right)^2 + COP'^2_z} + \sqrt{(COP'_x - L)^2 + \left(COP'_y - \frac{W}{2}\right)^2 + COP'^2_z} = N_8 - \frac{N_9}{EA} \quad (18B)$$

$$N_{10} \sqrt{COP'^2_x + \left(COP'_y - \frac{W}{2}\right)^2 + COP'^2_z} + \sqrt{(COP'_x - L)^2 + \left(COP'_y - \frac{W}{2}\right)^2 + COP'^2_z} = N_{11} - \frac{N_{12}}{EA} \quad (18C)$$

After we find the deformed COP location COP_x', COP_y', and COP_z', we substitute them back into Equations 14-17 and calculate the internal forces F_A, F_B, F_C, and F_D that causes this deformation. As it turned out, these forces are very sensitive to the precise COP location. We had to carry COP calculation to the 7th decimal point (i.e. ~1/*EA*) in order for the resultant forces *Drag*, *SideForce*, and *Downforce* to be within 1% of the computed values from CFD.

After computing the internal forces F_A, F_B, F_C, and F_D we note that they are equal-and-opposite of the tire reaction forces because each leg is a two-force member and the structure is modelled as a simple truss. This is the simplest structure we can think of to model this problem: using one externally applied force and four rods connecting it to the four tire contact patches.

3. Results

First, the starting point of this analysis is the output of the CFD simulations performed on the three cars. These were done separately over the past three years and published previously. The imported data is summarized in Table 1. Aside from changing the inlet boundary conditions so that the fluid velocity is 80.5 km/h (50 mph) with a yaw angle of 7.5°, the mesh and the turbulence model used is essentially the same as in the earlier studies. Because the three cars are simulated with the same flow condition, now they are directly comparable. One thing to note about the COP calculation in STAR-CCM+: this feature was introduced in Release 2020.3 of the software, under the *Center of Loads* report [11]. Earlier versions of STAR-CCM+ does not have this feature so we had to reload the earlier result files into Release 2020.3 in order to read out the COP

location. The COP location shown here is in the *center coordinate system*.

Table 1 Imported data from CFD.

	Williams FW42	Ferrari SF70H/71H	SJSU SR-12B
Drag	375.4 N	387.5 N	468.5 N
SideForce	-144.0 N	-145.6 N	-178.8 N
Downforce	-397.2 N	-492.7 N	-940.1 N
COP_x	1.191 m	1.698 m	0.736 m
COP_y	0.028 m	-0.064 m	-0.020 m
COP_z	0.851 m	0.775 m	0.465 m

3.1 CFD simulation summary

The starting point of this analysis is to perform CFD simulation to find the pressure distribution and the integral forces. The CFD simulations are performed using Siemen's STAR-CCM+ CFD software. The three car geometries are obtained from following sources: SJSU's Formula SAE car is own work, from the author's involvement in the Formula SAE team; William FW42 geometry is obtained from GrabCAD with creator's permission for reuse [12]; Ferrari SF70H/71H geometry is purchased from an artistic rendering website, with additional work requested to add a driver model into this high-fidelity car model. Each car is meshed separately, with the Ferrari model taking the longest because it's a surface model that wasn't meant for CFD analysis but rather for gaming.

The mesh of the three cars are shown in Figures 3-5. The mesh is generated using the automesher in STAR-CCM+. The type of mesh generated is cut-cell mesh. While cut-cell was easier to generate than tetrahedral or poly hexcore mesh, it was still non-trivial to generate these complex meshes, especially the Ferrari

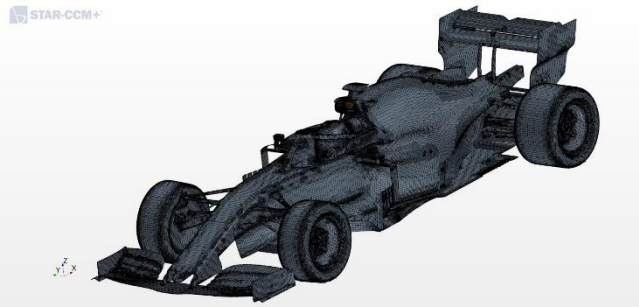

Figure 3. Williams FW42 mesh.

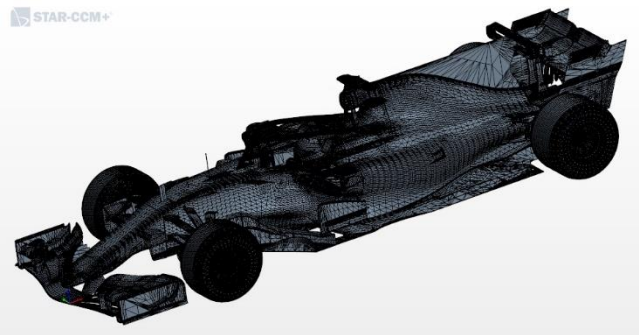

Figure 4. Ferrari SF70H/71H mesh.

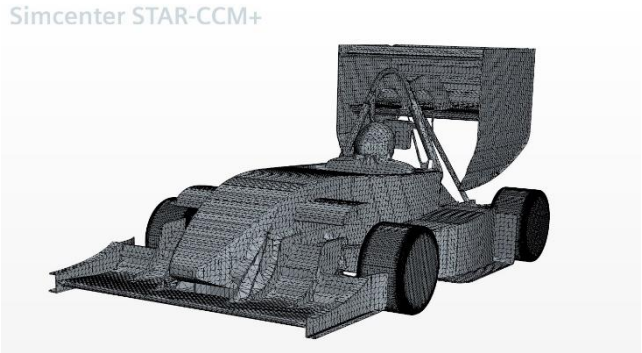

Figure 5. SJSU SR-12B mesh.

mesh. The Ferrari mesh took several months to get it to mesh because of slivers and intersections in the surface model which required a lot of surface repair. For each of the three cars, the mesh size that's generated is: 45 million elements for the Ferrari model; 14 million elements for the Williams model; 53 million elements for the SJSU FSAE model.

After a mesh is generated we move on to the solution phase. First thing in solving these meshes is to apply a boundary condition. For these computational grids we input an oblique flow of 7.5° to simulate a turning yaw, and an inlet velocity of 80.5 km/h (50 mph). The way we performed this yaw simulation is by changing the boundary condition instead of turning the car inside the computational domain. This way, the drag force we measure is still parallel to the car axis. An example of the flow orientation with respect to the computational domain is shown in Figure 6. The unusual boundary condition that we used here is to specify the front and the rightside walls as inlet and the leftside and the backwalls as outlet. The velocity is specified as a vector quantity instead of face-normal so it applies to both inlet walls. However, now the velocity magnitude has a normal component and a side flow component that had to be manually calculated beforehand. Other boundary conditions applied are rolling tires and a moving ground plane [13]. In this case, the velocity of the moving ground plane is also specified at an angle to the car. The surface of the cars are applied a no-slip boundary condition [14], with inflation prismatic layers to simulate boundary layer effect. Because of the cars' proximity to ground we also applied a prismatic layer to the ground plane to simulate ground effect. Ground effect vehicles such as the Soviet era *Ekranoplan* [15, 16] is not well understood and deserve more study. Perhaps it has to do with the suppression of natural turbulence formation?

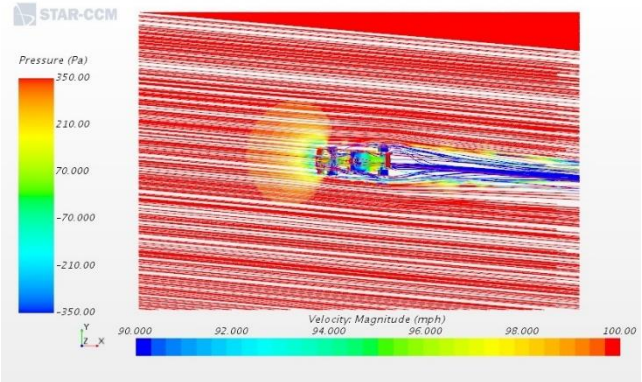

Figure 6. Topview of the flow orientation with respect to the computational domain.

Next on solution, a pressure-based solver is used, and a velocity-inlet and a pressure-outlet boundary condition is prescribed. The turbulence model used is σ-ω SST (shear-stress transport) [17]. All three car models are ran to 1000 iterations and stopped. At 1000 iterations the residuals have already stabilized, indicating that for the given mesh geometry this is as far as the solver will go. The typical run time for each car is about one full day on a 16 core CPU with 64 GB of RAM. The total *Drag*, *SideForce*, and *Downforce* reports are read out as well as the *center of loads* report that is computed by the CFD program. Because the result we need for the next step of analysis is quantitative, we simply extracted data from the *Reports* compiled by the software directly; plots generated by the post-processor for visualization are not shown here. The reader is redirected to reference [18, 19] for post-processor outputs of contour plots and streamlines.

3.2. Finding COP-Axis

The location of the COP-Axis is found by combining the *Drag*, *SideForce*, and *Downforce* components into a resultant force vector F_T, then moving it around in a plane that's perpendicular to the force vector F_T until the moments along the other two axis disappear [20]. All that remains is F_T and the residual moment M_T which is oriented along F_T.

To prove that this was done correctly, first when the resultant force vector F_T is moved in the plane perpendicular to F_T, M_T stays constant while the moments along the other two axis diminish. The COP-Axis that is found is plotted in Figure 7-9.

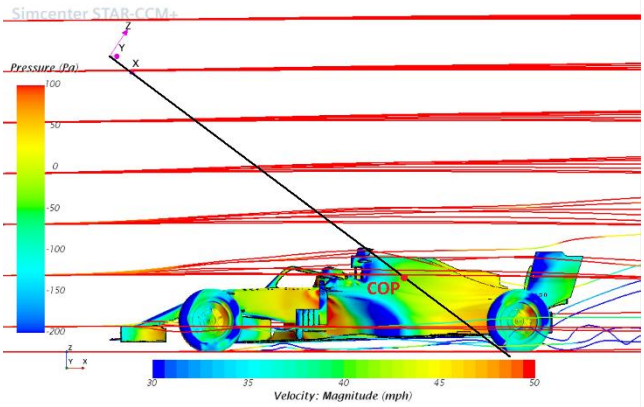

Fig. 7 COP-Axis of Williams FW42.

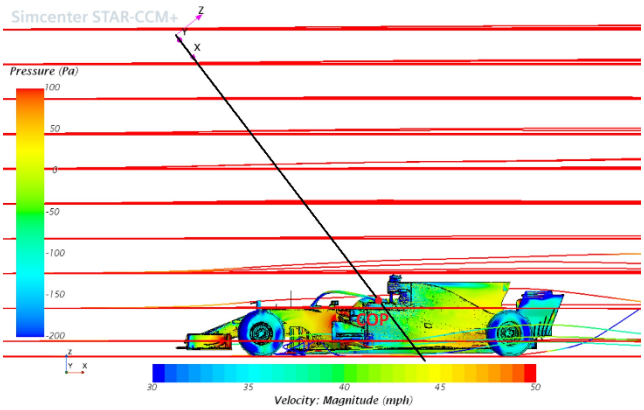

Fig. 8 COP-Axis of Ferrari FW70H/71H.

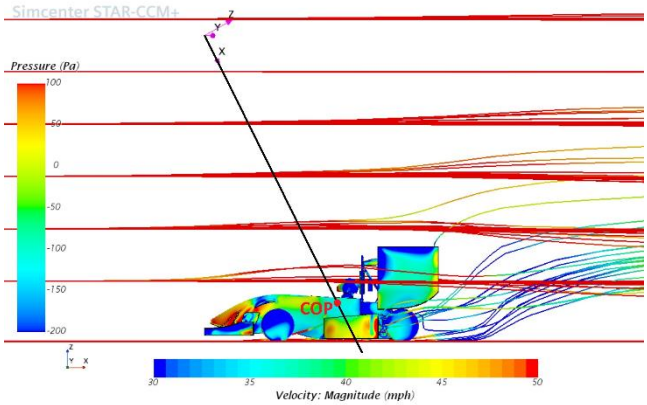

Fig. 9 COP-Axis of SJSU SR-12B.

Second, after we found the COP-Axis coordinates by manually moving it around on the car coordinate plane, the results are compared to the *center of loads* reported by the CFD software. Since the equation of a line in 3D space in vector form is

$$(x, y, z) = (x_o, y_o, z_o) + t(a, b, c) \tag{19}$$

we can use this to confirm the axis we found is the same as what's reported by CFD. Here, we use the *center of loads* coordinate identified by the CFD software as the LHS (x, y, z), use the newly found origin when we moved around the F_T vector as the RHS (x_o, y_o, z_o), and the direction unit vector (a, b, c) of $\overrightarrow{F_T}$. Then we calculate the *t*'s that will hold Equation 19 true. By calculating a *t* for each component of Equation 19, if they are equal then we know the *center of loads* reported by CFD software lies on the COP-Axis we identified and plotted in Figures 7-9. We verified that the reported *center of loads* fall right on the COP-Axis, thereby confirmed the COP-Axis we identified in section 3.2 are correct.

3.3. Static calculation results

Once the COP-Axis is found, next the static calculation is used to find the aero balance. This is easy since we are only summing forces and moment from external loads (i.e. resultant force F_T, and the tire reaction forces F_A, F_B, F_C, and F_D) and setting them equal to zero; no internal forces or deformations are needed. Doing this gives us a combination of forces from tires A, B, C and D. With these, we can calculate the aero balance "front vs. rear" and "inside vs. outside." Keep in mind that all three cars are simulated at the same velocity and the same yaw angle, therefore the data depends only on their shape and therefore are comparable.

Table 2 Aero balance.

	Williams FW42	Ferrari SF70H/71H	SJSU SR-12B
Front/Rear	42.8 / 57.2	32.6 / 67.4	36.2 / 63.8
Inside/Outside	32.5 / 67.5	31.7 / 68.3	41.2 / 58.8

3.4. Solid mechanics calculation results

To go one step further, solid mechanics and the method of deformation is used to find individual tire reaction forces. The result of the solid mechanics calculations are shown in Tables 3-5. Table 3 is the tire reaction forces for Williams FW42. Table 4 is

the tire reaction forces for Ferrari SF70H/71H. Table 5 is the tire reaction forces for SJSU's SR-12B.

Table 3 Tire reaction forces for Williams FW42.

	F_A	F_B	F_C	F_D
x-component	-195.7 N	-41.8 N	267.8 N	345.2 N
y-component	-136.6 N	27.1 N	90.7 N	-125.0 N
z-component	-139.7 N	-29.8 N	-99.2 N	-128.1 N

Table 4 Tire reaction forces for Ferrari SF70H/71H.

	F_A	F_B	F_C	F_D
x-component	-273.1N	-78.7 N	266.9 N	472.0 N
y-component	-117.9 N	40.0 N	133.4 N	-201.1 N
z-component	-124.6 N	-36.0 N	-120.1 N	-212.2 N

Table 5 Tire reaction forces for SJSU SR-12B.

	F_A	F_B	F_C	F_D
x-component	-334.5 N	-204.6 N	433.7 N	573.8 N
y-component	-270.5 N	176.1 N	352.3 N	-437.3 N
z-component	-211.3 N	-129.0 N	-258.0 N	-341.6 N

To prove that these forces are calculated correctly, when the *x, y,* and *z*-components are added together they are equal to the *Drag*, *SideForce*, and *Downforce* from CFD simulation. This is within 1% of CFD prediction, because as we have seen that this result is highly sensitive to the precision, and only when we carried it to the seventh decimal place (i.e. 1/*EA*) did we get the numbers to match. The value of *EA* used here is 29,000 kips (128,998 kN). This is only an estimate and is chosen out of convenience, without loss of generality in illustrating this analysis technique. The modulus of steel is 29 Msi (200 GPa), and we use a unit area of 1 square inch (6.45 cm^2). As mentioned earlier, the precise *EA* should come from an FEA of the chassis.

When we compare the solid mechanics result to the static calculation result, if we ignore the residual torque value M_T because it's usually small, the aero balance we would get is exactly the same as what's shown in Table 1 [21]. Also, because our pyramid model is a simple truss (or space truss since it's in 3D), it is comprised of two-force members and pin joints. Therefore, it does not support externally applied moments and there would be no bending in two-force members. An analytical model that supports bending would be a great enhancement to the foregoing research.

4. Discussion

The contribution of this paper is in the methodology to compute individual tire forces. The CFD of the three cars used here are simply for example to carry out this methodology. However, for completeness we will say the following:

4.1. Discuss aero balance results

First, from the static calculation and the results summarized in Table 2, it reported that Williams FW42 has the best front/rear aero balance and that SJSU's SR-12B has the best inside/outside aero balance. This is surprising because based on race record, Ferrari SF70H had a great winning streak in 2017 while the Williams FW42 had trouble from the start in 2019. It is hard to imagine that this Ferrari design would have worse aerodynamics than Williams. Also, the SJSU SR-12B is a collegiate SAE student competition while Formula 1 is professional motorsport [22-24], it's hard to believe that it would have better inside/outside aero balance. The analysis yielded results that are counterintuitive, but as we say: it is what it is; we'll attribute this to the inaccuracies of the CFD computed forces that were done at different times [25-27]. But one theory we can offer for SJSU's SR-12B is that it has a much narrower trackwidth so perhaps that contributed to the inside/outside aero balance. Another thing to point out is that these simulations were done at one particular speed (80.5 km/h or 50 mph) and one yaw angle (7.5°) so it only represents a snapshot in time. In reality, when the cars are going through a corner, the yaw angle and hence the COP [28, 29] is constantly changing along with the speed, so more simulation is needed in order to paint a complete picture and allow a complete "turn-in, apex, and exit" analysis and comparison.

4.2. Discuss individual tire results

Next, from the solid mechanics calculation and the results shown in Tables 2-4, the individual tire reaction loads are revealed in three coordinate components. While it's good to go down to this level of granularity, this information may not be practical because it would be too academic. The individual tire information may not be of interest to a vehicle dynamicist, but maybe only be useful to the tire engineer. When the cars are yawing 7.5 degrees to the right, the aerodynamic load is transmitted to the outside tires (i.e. driver's left). This aerodynamic load on the tires is in addition to the weight of the car and also to the weight-shifting when the car is going around a corner. Let me reiterate -- this additional force on the tire is purely from aerodynamics alone; in other words, if the cars were running with no aerodynamic modifications, these forces should be zero even when cornering.

Now that we have a way to compute individual tire forces, utilizing the same inputs (i.e. vehicle speed and yaw angle) and computing the same output metrics (i.e. transmitted reaction forces to each tire), it makes sense to compare the effectiveness of different aerodynamic designs -- for the benefits in cornering. From a vehicle dynamics perspective, perhaps it's not so important to know the exact force on each tire; knowing the aero balance in terms of the front/rear distribution and the inside/outside distribution will tell us more. The front/rear distribution will tell us the amount of oversteer or understeer the vehicle will experience. The inside/outside distribution will tell us the effectiveness of aerodynamic force in helping with cornering. More force that's transferred to the inside tires will be beneficial as evident in sidecar racing as shown in Figure 10 [30] and in yacht racing [31]. Because of this, knowing the individual tire reaction force is merely academic; however, we've shown that the combined tire loads from the deformable body calculation does indeed equal the % tires ratio from the static moments calculation. This is verification that our calculation was done correctly.

Source: NK Photography

Fig. 10 Adding weight to inside tire in sidecar racing.

4.3. What would make this research better

To remove the ambiguity of CFD results it would have been better if we analyzed all of them with the same mesh density, the same mesh quality (i.e. orthogonality or skewness), and the appropriate boundary layer thickness (i.e. $y+$). In hindsight, a better way to illustrate this methodology would be to use a simple shape such as the Ahmed model [32, 33], so we wouldn't need to worry about geometry complexity and question the CFD accuracy. However, the reason why we ran such complex and photorealistic models in the first place is because these models are hard to comeby in the motorsport industry [34, 35], and being able to mesh and solve them offer a different perspective.

Lastly, during the deformable body calculation, numerous Excel spreadsheets were used to compute the point-cloud in order to numerically solve the system of nonlinear equations. Leaving it to the readers, it would be further improvement if mathematically a close-form solution can be found so that we wouldn't need to resort to solving it numerically.

5. Conclusion

A way to compute the transmitted tire force from the aerodynamic force has been presented in this paper. The methodology has been demonstrated for three cars. The three cars were simulated using the same velocity and the same yaw angle as required to make the three cases comparable.While CFD results were shown, these results are just application samples and do not show the actual performances due to the insufficient accuracy of input data. Utilizing the aerodynamic forces generated, combining with the location where these forces should be applied, the transmitted aerodynamic force to the tires have been calculated. The difficulties in solving a static indeterminant problem and the resulting nonlinear equations had been resolved. Using this metric of transmitted tire force, the effectiveness of the aerodynamic design in cornering performance can be determined. By using the method presented in this paper, a comparison can be made between different car shapes and select the one that transmits more loads to the inside tires.

6. Acknowledgments

This research has been conducted as a part of the project for SJSU Formula SAE team and as the author's graduate studies work under Prof. Papadopoulos.

References

(1) Brown, J., Robertson, A.J., and Serpento, S., Motor Vehicle Structures: Concepts and Fundamentals, Butterworth-Heinemann Publishing, 2002.
(2) Beer, F. and Johnston, E.R., Jr., Vector Mechanics for Engineers, 5th Edition, McGraw-Hill Book Company, 1988.
(3) Mahdi Al-Obaidi, A., and Sun, L., Calculation and Optimization of the Aerodynamic Drag of an Open-wheel Race Car, Journal of Engineering Science and Technology EURECA, 2014.
(4) Swokowski, E.W., Calculus with Analytic Geometry, 2nd Edition, PWS-KENT Publishing Company, pp.598-599, 1988.
(5) Formula1-dictionary.net, https://www.formula1-dictionary.net/aerodynamic_balance.html, accessed March 1, 2022.
(6) Totalsim UK website, https://www.totalsimulation.co.uk/secrets-formula-1-part-2-importance-aerodynamics/, accessed March 1, 2022.
(7) Kyle.Engineers YouTube video, How Does Aero Balancing Work? Centre of Pressure Explained, https://www.youtube.com/ watch?v=Y68hebQ4npE, accessed March 1, 2022.
(8) Pinheiro, H. D. C., Ferraris, A., Messana, A., Carello, M., et al., Integrated Design and Control of Active Aerodynamic Features for High Performance Electric Vehicles, SAE Technical Paper 2020-36-0079E, doi: 10.4271/2020-36-0079, 2020.
(9) Zavatsky, A.B., Lecture 3: Statically Indeterminate Structures, University of Oxford, Supplementary Lecture Handouts, 2007.
(10) Crandall, S., Dahl, N., and Lardner, T., An Introduction to the Mechanics of Solids, 2nd Edition, McGraw-Hill Inc., 1978.
(11) How to find the Center of Pressure, https://community.sw.siemens.com/s/article/How-to-find-Center-of-Pressure, accessed July 19, 2021.
(12) N. Dhillon, Reuse Permission, https://grabcad.com/, October 18, 2019.
(13) Turner, T. R., Wind-tunnel Investigation of a 3/8-scale Automobile Model over a Moving-belt Ground Plane, NASA TN D-4229, NASA Langley Research Center, 1967.
(14) Anderson, J. D., Jr, Fundamental of Aerodynamics, 5th Edition, 2011.
(15) Ekranoplan, https://en.wikipedia.org/wiki/Lun-class_ekranoplan, accessed March 5, 2022.
(16) I. de Oliveira and L.F. Paulinyi, Aerodynamic Study of Formula 1 Wing in Ground Effect using Computational Fluid Dynamics, 24th ABCM International Congress of Mechanical Engineering, Curitiba, Brazil, December 3-8, 2017.
(17) Menter, F. R., Kuntz, M., Langtry, R., Ten Years of Industrial Experience with the SST Turbulence Model, Turbulence, Heat and Mass Transfer, 4, 2003.
(18) Lin, M. and Papadopoulos, P., High-Fidelity Geometry, Fault-Tolerant Meshing, Resolving Runtime Errors in Motorsport CFD Applications, Proceedings of the 29th Annual Conference of the Computational Fluid Dynamics Society of Canada, Online, 2021.
(19) Lin, M. and Papadopoulos, P., Effect of Halo Protection Device on the Aerodynamic Performance of Formula Racecar, ICAMME 2020: 14. International Conference on Automotive, Mechanical and Materials Engineering, London, UK, pp.1297-1301, 2020.
(20) FSAE Discussion Forum: Cars with wings, http://www.fsae.com/forums/showthread.php?10551-Cars-with-wings/page2&s=4ab1fc7312d322e0f54236b19c27169c, Thread #11-40, 2012
(21) Widyastuti, Kusuma, R., Rochiem, R., and Pramujati, B., Center of Pressure Analysis for Bullet Angle of Attack using

Computational Fluid Dynamic, AIP Conference Proceedings 2384, 030007, 2021.
(22) Toet, W., Aerodynamics and Aerodynamic Research in Formula 1, The Aeronautical Journal, 117(1187), 1-26. doi:10.1017/S000 1924000007739
(23) Bienz, C., Larsson, T., Sato, T., Ullbrand, B., In Front of the Grid - CFD at SAUBER PETRONAS F1 Leading the Aerodynamic Development, European Automotive CFD Conference, 2008.
(24) Ogawa, A., Yano, S., Mashio, S., Takiguchi, T., Nakamura, S., Shingai, M., Development Methodologies for Formula One Aerodynamics, Honda R&D Technical Review, F1 Special (The Third Era Activities), pp. 142-151, 2009.
(25) Williams, M. and Shires, A., Validation of CFD for Racing Car Analysis and Design, SAE Technical Paper 2002-01-3349, doi:10. 4271/2002-01-3349, 2002.
(26) Ueno, D., Hu, G., Komada, I., Otaki, K., et al., CFD Analysis in Research and Development of Racing Car, SAE Technical Paper 2006-01-3646, doi:10.4271/2006-01-3646, 2006.
(27) Desai, M., Channiwala, S., and Nagarsheth, H., Computational Validation of Experimental Aerodynamic Predictions of a Car, International Conference on Fluid Mechanics and Aerodynamics, pp. 125-128, 2008
(28) Center of Pressure - cp, NASA Glenn Research Center, https://www.grc.nasa.gov/www/k-12/airplane/cp.html, accessed September 16, 2021.
(29) Generating a Force, Moment, or Center of Pressure Report, ANSYS Tutorial, https://www.afs.enea.it/project/neptunius/docs/fluent/html/ug/node962.htm, accessed March 5, 2022.
(30) FIM Sidecar World Championship, https://en.wikipedia.org/wiki/Sidecar_World_Championship, accessed February 18, 2022.
(31) Yacht racing, America's Cup, https://en.wikipedia.org/wiki/America%27s_Cup, accessed February 18, 2022.
(32) Ahmed, S.R., Ramm, G., Some Salient Features of the Time-Averaged Ground Vehicle Wake, SAE-Paper 840300, 1984
(33) Strachan, R. K., Knowles, K., and Lawson, N. J., A CFD and Experimental Study of an Ahmed Reference Model, SAE Technical Paper, doi:10.4271/2004-01-0442, 2004.
(34) Katz, J., Race Cars Aerodynamics, 2nd Edition, Bentley Publishers, 2006.
(35) Katz, J., email communication, January 25, 2020.